Cepheid Stars: An Orbital Arrival-Time Model for Periodic Luminosity Variations

A quantitative case study of δ Cephei with a luminous binary component, Gaussian arrival-time broadening, and a faint extended environment

Complete working manuscript • 24 November 2026

Scope. This paper demonstrates how stars with constant intrinsic luminosity may be observed as periodically pulsating light sources if the velocity of the emitting source influences the propagation velocity of light. Under the proposed (c+u) model, orbital motion changes the arrival-time distribution of electromagnetic radiation, producing periodic variations in observed brightness without requiring physical expansion, contraction, or intrinsic luminosity oscillations of the stars. The study presents a quantitative orbital model of δ Cephei and compares its predicted light curve with astronomical observations.

Abstract

We examine whether an orbiting stellar component can generate a periodic, asymmetric apparent light curve through a proposed ballistic arrival-time relation in which light emitted by a source with line-of-sight velocity u propagates at c+u. The hypothesis is explored as a quantitative alternative to attributing the photometric variability of a Cepheid solely to periodic radial expansion and contraction. The demonstration adopts a luminous component A of 1.5 solar masses, a faint gravitational companion B of 1.2 solar masses, and an eccentric 5.366531-day orbit. Arrival-time compression converts the periodic radial acceleration of A into a nonuniform distribution of received light. A Gaussian response of width 0.530 days describes unresolved broadening of the ideal signal; a small constant flux represents diffuse or unresolved light. When the eccentricity is fitted to a published Johnson-V Fourier template for δ Cephei, the best solution obtained in our exploration has e ≈ 0.419, inclination i ≈ 0.338°, background flux ≈ 0.225 times the mean light of A, and a root-mean-square magnitude difference of approximately 0.013 mag relative to that smoothed empirical template. The resulting model matches the dominant photometric period, amplitude, and rise/decline asymmetry. We discuss plausible broadening mechanisms, the role and limits of an extended disk, and key constraints from interferometry and radial-velocity spectroscopy. The present result establishes a successful parametric light-curve fit within the assumed c+u kinematics, while identifying the additional observational tests needed before a physical interpretation can be accepted.

Keywords: Cepheid variables; δ Cephei; binary dynamics; arrival-time concentration; asymmetric light curves; Gaussian broadening; alternative kinematic models.

1. Introduction

Classical Cepheids exhibit stable, characteristic brightness cycles and occupy a central place in stellar astrophysics. In the standard physical interpretation, periodic changes in radius, temperature, and atmospheric velocity lead to the observed variability. Their period–luminosity relation provides a crucial distance indicator. The prototype δ Cephei has an optical period of approximately 5.366 days and a strongly asymmetric V-band light curve: brightness increases comparatively rapidly and decreases more gradually [1, 2].

An alternative explanation must not merely generate a periodic signal. It must account for the cycle duration, profile asymmetry, optical amplitude, coherence of successive maxima, and independent observables such as phase-dependent spectral-line velocities and interferometric angular diameters. These constitute distinct empirical constraints on any proposed physical model [3–6].

The present paper asks a deliberately narrower but quantitative question. Assuming a source-velocity-dependent propagation law c+u, can ordinary Keplerian motion in a compact binary produce a received light curve close to the observed morphology of δ Cephei? We construct one example and quantify its agreement with a published Fourier reconstruction of AAVSO Johnson-V observations [2]. We do not search the full population of possible multiple-star systems or claim to identify the actual components of δ Cephei.

The proposed construction is composed of (i) a luminous central star A, (ii) a faint or dark gravitating body B, and (iii) a possible surrounding distribution of low-contrast light. It is the timing of the radiation from A, rather than its imposed periodic intrinsic power variation, that gives rise to the primary photometric signal. A compact mathematical parameterization is used to separate the proposed kinematic mechanism from uncertain source-surface and environmental details.

2. Physical Concept and Model Boundaries

2.1 Central binary and extended environment

Component A is the dominant time-dependent luminous source. Component B supplies orbital acceleration while contributing negligible direct optical light in the selected model. A circumbinary disk or diffuse stellar environment may contribute weak and slowly varying flux. The present photometric result does not require a unique identification of the environment: it enters chiefly through a net additive flux and can later be subjected to interferometric or spectral tests.

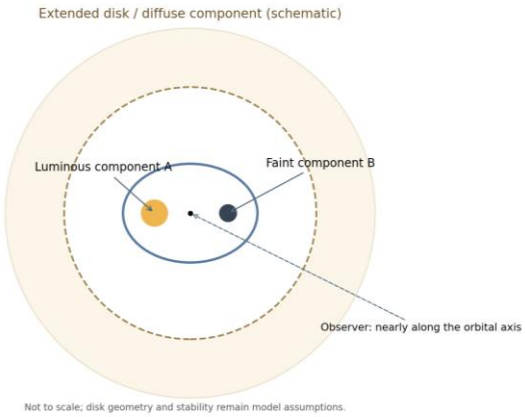


***Figure** 1. Schematic structure of Model A: the luminous star A follows an eccentric orbit around the common center of mass with a faint body B. A possible extended disk or environment contributes low-contrast light. The illustration is conceptual and is not a dynamical reconstruction.*

2.2 Distinguishing intrinsic luminosity from received flux

We assume that the emitted power of A is approximately steady on the orbital timescale, and that the measured light curve is modified by nonuniform arrival times. In an emission interval dt, a fixed amount of emitted optical energy is redistributed into an arrival interval dt_arr. In the simplest lossless model, this gives a received flux proportional to the inverse Jacobian |dt_arr/dt|. Multiple emission epochs that map to the same arrival time contribute additively. This distinction between intrinsic emitted luminosity and

observed arrival-time density is central to the proposed mechanism.

The c+u law is an explicit hypothesis of this article, not a consequence derived from vacuum Maxwell equations. A successful phenomenological fit under this hypothesis must therefore be evaluated separately from whether the propagation law applies to astronomical radiation. The following sections define exactly which mapping is used so that the calculation can be independently reproduced.

2.3 Geometric variables and sign convention

Let D be the distance to the observer, x(t) the displacement of A toward the observer, u(t)=dx/dt its line-of-sight speed, and a_los(t)=du/dt its acceleration. A positive u means motion toward the observer. The orbit is viewed close to face-on; inclination i is measured from the face-on orientation. The line-of-sight component is therefore proportional to sin i. Unlike the relative Keplerian velocity, u in the arrival-time law belongs to the emitting body itself.

3. Keplerian Motion of the Inner Pair

3.1 Adopted masses, period, and eccentricity

For the numerical case study we use M_A=1.5 M_sun, M_B=1.2 M_sun, P=5.366531 d and e=0.418673. The masses are model choices; they have not been inferred from a dynamical orbit of δ Cephei. The period is fixed to the photometric reference value. Eccentricity and inclination are selected through the light-curve fitting process.

$$n = \frac{2\pi}{P}, \quad a^3 = \frac{G(M_A+M_B)}{n^2} \quad (1)$$

$$a_A = \frac{aM_B}{M_A+M_B}, \quad a_B = \frac{aM_A}{M_A+M_B} \quad (2)$$

The Keplerian semimajor axis of the relative orbit is a≈17.962 R_sun; the semimajor axis of A around the barycenter is a_A≈7.983 R_sun. The minimum and maximum center-to-center separations are a(1−e)≈10.44 R_sun and a(1+e)≈25.48 R_sun. Physical component radii must remain consistent with the closest separation and with tidal or Roche constraints; these properties are not inferred solely from the photometric fit.

3.2 Orbital phase and projected motion

$$M(t) = n\left(t - t_{\mathrm{peri}}\right) = E - e\sin E \quad (3)$$

$$X = a(\cos E - e), \quad Y = a\sqrt{1-e^2}\sin E \quad (4)$$

We choose the line of nodes and periastron orientation so that the line-of-sight displacement of A is proportional to −Y. This convention specifies the phase at which the largest positive line-of-sight acceleration occurs; an arbitrary initial epoch introduces only a horizontal shift in the phase-folded model.

$$x_A(E) = -\frac{M_B}{M_A+M_B}\, a\sqrt{1-e^2}\sin E \sin i \quad (5)$$

$$u_A(E) = -\frac{M_B}{M_A+M_B}\, \frac{an\sqrt{1-e^2}\cos E \sin i}{1-e\cos E} \quad (6)$$

$$a_{\mathrm{los}}(E) = \frac{M_B}{M_A+M_B}\, \frac{an^2\sqrt{1-e^2}\sin E \sin i}{(1-e\cos E)^3} \quad (7)$$

These expressions follow from the two-body Kepler equations and are evaluated at uniformly sampled emission times. E is solved iteratively from Kepler's equation. The measured photometric phase is determined from the arrival-time sequence, not directly from the orbital anomaly.

3.3 Critical acceleration and viewing angle

In the c+u mapping, the approximately critical radial acceleration depends primarily on distance rather than on the orbital period. For the illustrative adopted distance D=890 light-years, a_crit=c^2/D≈0.010674 m s^{-2}. The chosen inclination is defined so that the maximum positive projected acceleration reaches 1.05 a_crit; this gives i≈0.338°. The 5% excess above critical is a modeling condition, not a directly measured property of δ Cephei.

$$a_{\mathrm{crit}} = \frac{c^2}{D}, \quad \max_t[a_{\mathrm{los}}(t)] = 1.05\, a_{\mathrm{crit}} \quad (8)$$

Parameter	Selected value	Role
P	5.366531 d	Observed photometric

		period used as input
M_A	1.5 M_sun	Illustrative luminous component mass
M_B	1.2 M_sun	Illustrative companion mass
e	0.418673	Photometric shape parameter
i	0.338080°	Controls projected acceleration
D	890 light-years	Adopted propagation baseline
a	17.962 R_sun	Derived relative semimajor axis

4. Arrival-Time Compression with c+u

4.1 Exact timing relation used in the calculation

The assumed arrival time of light emitted at t is

$$t_{\mathrm{arr}}(t) = t + \frac{D - x_A(t)}{c + u_A(t)} \quad (9)$$

This expression reduces to a constant flight time plus t when x and u vanish. Differentiation gives

$$\frac{\mathrm{d}t_{\mathrm{arr}}}{\mathrm{d}t} = \frac{c}{c+u_A} - \frac{(D-x_A)a_{\mathrm{los}}}{(c+u_A)^2} \quad (10)$$

A local concentration of arrival times occurs when this derivative becomes small. In the idealized zero-width description, the inverse Jacobian can become very large and, beyond a fold, several emission times can map to the same arrival time. This is an arrival-time caustic in the assumed kinematics, not a gravitational lens caustic.

4.2 Flux conservation under a time mapping

Let L_A be the temporally steady emitted power in the band of interest. For each arrival time t_arr, the idealized source-dependent response is obtained by summing the contribution from all emission times t_j satisfying the arrival-time equation:

$$F_{A,0}(t_{\mathrm{arr}}) \propto \sum_j \frac{L_A}{\left|\mathrm{d}t_{\mathrm{arr}}/\mathrm{d}t\right|_{t_j}} \quad (11)$$

Numerically, instead of directly dividing by the Jacobian near its zeros, we emit equal-energy samples at equally spaced t, transform them to t_{arr}, accumulate them into phase bins, and normalize to unit mean. This histogram method automatically includes multiple arrival branches. Fluxes remain finite after application of the response kernel in Section 5.

4.3 Stable numerical evaluation

Subtracting two huge light-travel times can create significant floating-point cancellation when D is astronomical. We therefore calculate only the arrival offset relative to the constant D/c propagation time, using the algebraically stable expression

$$\delta t(t) = -\frac{c\,x_A(t) + D\,u_A(t)}{c[c+u_A(t)]} \quad (12)$$

$$t_{\mathrm{arr,rel}} = t + \delta t(t) \quad (13)$$

The values are folded modulo P after converting the offsets to days. The procedure is valid within the adopted ballistic timing assumption and is straightforward to reproduce with standard numerical tools.

4.4 Why eccentricity changes pulse asymmetry

In a circular orbit, the radial acceleration is sinusoidal, and a near-critical compression tends to produce an approximately symmetric brightening. Nonzero eccentricity breaks this temporal symmetry: both the magnitude of the orbital acceleration and the rate at which it changes vary strongly around the orbit. The resulting arrival-time density acquires a faster and a slower branch. In the explored configuration, eccentricity is therefore a principal shape parameter, while the inclination mainly selects proximity to the critical timing condition.

5. Gaussian Broadening of the Received Pulse

5.1 Motivation for an effective response kernel

The ideal caustic response is sharper than the observed mean light curve. A finite emitting region, distribution of projected velocities, nonuniform intensity, surface rotation, local atmospheric motions and several propagation or processing effects may spread the arrival times. Rather than attribute the observed width to a unique mechanism without independent evidence, we represent their combined impact using a Gaussian timing response of width σ. This is a deliberately effective description, not an identified physical surface process.

$$G_\sigma(\tau) = \frac{1}{\sqrt{2\pi}\sigma}\exp\left(-\frac{\tau^2}{2\sigma^2}\right) \quad (14)$$

$$F_A(t) = \int_{-\infty}^{\infty} F_{A,0}\,(t-\tau)G_\sigma(\tau)\,\mathrm{d}\tau \quad (15)$$

All convolutions are evaluated periodically over the full 5.366531-day cycle. By construction, the kernel conserves the mean of the modeled stellar flux; it redistributes that flux over arrival phase rather than introducing a net luminosity gain.

5.2 Why the Gaussian parameter is retained

Our earlier tests substituted the rotational broadening kernel of a uniformly bright disk for the Gaussian response and subsequently introduced a linear limb-darkening law. Rotational broadening generated part of the required pulse width but did not match the full observed morphology as closely at the fixed fitted orbital parameters. The RMS magnitude difference was approximately 0.0425 mag for a uniform projected disk and 0.0318 mag for the strongest tested linear limb darkening, compared with approximately 0.013 mag for Gaussian broadening. These tests demonstrate that surface weighting matters, but they do not uniquely identify the source of the broadening.

In the present paper, σ is therefore left as a fitted effective timescale. Its value is not converted into a single asserted rotation rate or a unique stellar radius. A later multi-parameter surface model may be able to explain it dynamically, and such models can be tested using time-resolved line shapes and wavelength dependence.

5.3 Relation to velocity dispersion in the assumed propagation law

For |u| much smaller than c and a distant source, a small difference δu in radial emission velocity produces an approximate arrival-time offset $\delta t \approx -D\ \delta u/c^2$. Consequently, a Gaussian timing width σ_t would correspond to a formal radial-velocity dispersion $\sigma_u \approx (c^2/D)\sigma_t$. At D=890 light-years and σ_t=0.530 d this gives $\sigma_u \approx 0.489$ km s^{-1}. This is a useful scale, not a measurement of turbulent or rotational surface velocities.

$$\sigma_u \approx \frac{c^2}{D}\sigma_t \approx 0.489\ \mathrm{km\,s^{-1}} \quad (16)$$

Finite geometric path differences by themselves do not provide the same broadening: a path length of 100 solar radii corresponds to only about 232 seconds of ordinary light-travel time. Any interpretation of σ as a projected-velocity distribution must be developed through a surface-resolved timing calculation.

6. Additional Flux and the Circumbinary Environment

6.1 Flux decomposition

The observed photometric signal is modeled as the broadened output of A plus a slowly varying or effectively constant contribution from unresolved components. The companion B is set to optically dark for the principal fit because allowing a small component B light curve did not materially improve the match, and larger B contributions degraded the fit.

$$F_{\mathrm{total}}(t) = L_A\, f_A(t; e, i, \sigma) + C L_A \quad (17)$$

where the normalized mean of f_A is one and the constant dimensionless C accounts for the combined disk and unresolved background. The zero-point of the V magnitude is fitted separately:

$$V_{\mathrm{model}}(t) = V_0 - 2.5\log_{10}\frac{F_{\mathrm{total}}(t)}{F_{\mathrm{ref}}} \quad (18)$$

In the preferred photometric fit, C≈0.225. Thus approximately C/(1+C)≈18.4% of the modeled cycle-averaged received optical flux arises from the constant component. This fraction is not independently predicted by disk radiative transfer; it is inferred from the amplitude constraint.

6.2 Extended radial brightness profile

The environmental component can be visualized as a disk with an inner radius, an outer radius, and a surface-brightness law I(r)∝r^(−p). A steep law allows an outer structure to extend farther than its dominant emitting region. For example, an illustrative disk extending from 30 to 100 solar radii has more than 90% of its own integrated light inside 45 solar radii if p≈8. This provides a possible geometric mechanism for separating material extent from observed brightness extent, but the chosen law has not been inferred from a thermal, scattering or hydrodynamic model.

$$F_{\mathrm{disk}} \propto 2\pi \int_{r_{\mathrm{in}}}^{r_{\mathrm{out}}} I(r) r \, \mathrm{d}r, \quad I(r) = I_0 \left(\frac{r_{\mathrm{in}}}{r}\right)^{p} \quad (19)$$

The circumbinary stability of the dense inner portion of such a disk is not established by the optical fit. Test-particle integrations conducted during model development found ordinary small-body circular orbits at radii 30–45 solar radii to be strongly disturbed by the eccentric binary, while substantially more distant test orbits fared better. A fluid or particulate disk requires a separate dynamical treatment including collisions, pressure, heating and replenishment; no stability proof is claimed here.

6.3 Energy balance and the role of reflected light

A disk may scatter or reprocess some light emitted by A. Passive reflection cannot generate more radiative energy than it intercepts. Reflected radiation also carries much of the intrinsic and arrival-time modulation of the illuminating source unless additional angular mixing or time-dependent transfer is present. Therefore C cannot be explained merely by assigning an arbitrary high reflectivity to a disk. The fitted constant flux can originate from intrinsic sources, reprocessed radiation under a specified geometry, or unresolved components, but its actual energy budget remains an independent constraint.

6.4 Interferometric apparent size

The mean angular diameter often quoted for δ Cephei is about 1.52 milliarcseconds, with phase-dependent interferometric measurements and extended circumstellar structure reported in the literature [4–6]. A bright ring and a limb-darkened stellar disk with the same external angular diameter do not have the same visibility function. Consequently, matching a geometric radius of roughly 45 solar radii is not equivalent to reproducing an interferometric observation. In the present article, the disk is a conceptual environment and its detailed interferometric visibility is retained as a quantitative follow-up test.

In particular, published visible-light interferometry has attributed an extended circumstellar component a contribution of roughly 7% in the relevant observing configuration [5]. Our inferred constant V-band contribution of about 18% cannot simply be identified with that observational component without accounting for bandpass, structure, spatial filtering and model dependence. The difference is an informative constraint rather than a reason to assign an unobserved disk flux without calculation.

7. Numerical Construction for δ Cephei

7.1 Reference photometric observations

As the empirical target we use the published three-harmonic Johnson-V Fourier reconstruction of Elahi and Gull (2026) [2]. The underlying AAVSO dataset contains 244 reported measurements, of which 242 were retained in their cleaned sample. The adopted period is 5.366531 d. The resulting smooth template has a full magnitude range of 0.854439 mag, a rise fraction of 0.2885 and a pronounced non-sinusoidal profile. It is important that this is a smoothed observational representation: its fit error must not be confused with the residual scatter of the individual 242 observations.

$$V_{\rm obs}(\phi) = c_0 + \sum_{k=1}^{3}[c_k\cos(2\pi k\phi) + s_k\sin(2\pi k\phi)] \quad (20)$$

Harmonic k	c_k (mag)	s_k (mag)
0	3.903085	—
1	−0.242286	−0.243384
2	−0.133974	−0.049481
3	−0.052745	+0.006366

The coefficients in Table 2 are reproduced from the public empirical template [2] and define the observational comparison used throughout the article. A phase offset and magnitude zero point are nuisance parameters, not physical properties of the proposed orbit.

7.2 Sampling, smoothing and fitting procedure

For each eccentricity, the Kepler equation is solved on a uniform grid of emission times spanning a full orbit. The barycentric line-of-sight velocity and displacement of A are evaluated analytically, and Equation (12) gives the arrival-time offset. The resulting arrival phases are accumulated into a high-resolution histogram. A periodic Gaussian filter of width σ is then applied, and a non-negative constant C is added. Finally, the modeled flux is converted to V magnitude; a circular phase shift aligns the modeled and observational profiles. The standard deviation of the phasewise magnitude residuals is used as the goodness-of-fit statistic.

$$\mathrm{RMS} = \sqrt{\frac{1}{N}\sum_j \left[V_{\rm model}(\phi_j) - V_{\rm obs}(\phi_j)\right]^2} \quad (21)$$

During the optimization the period and illustrative component masses are held fixed. The eccentricity e and Gaussian width σ are allowed to vary; inclination is recalculated from the near-critical acceleration condition, while C is adjusted to match the template amplitude. This produces a conditional optimum, not a fully identifiable inference of masses, distance, inclination and binary structure from the observations.

7.3 Preferred fit and input–output bookkeeping

Quantity	Value	Interpretation
Orbital period P	5.366531 d	Fixed from photometry
Mass M_A	1.5 M_sun	Assumed
Mass M_B	1.2 M_sun	Assumed
Eccentricity e	0.418673	Fitted
Inclination i	0.338080 °	Derived from critical-acceleration condition
Gaussian width σ	0.530185 d	Fitted
Background C	0.2254 L_A	Amplitude-calibrated
Empirical V amplitude	0.854439 mag	From [2]
Model/template RMS	0.0130 mag	Calculated against Fourier template

The central result is the agreement of the entire asymmetric light-curve morphology with only a modest background contribution. The fit is not merely a period match: the slow decline, broad minimum and rapid ascent are jointly reproduced to the quoted residual level. Because the period is prescribed and e, σ and C are adjusted, those quantities should not be presented as independent predictions of the model.

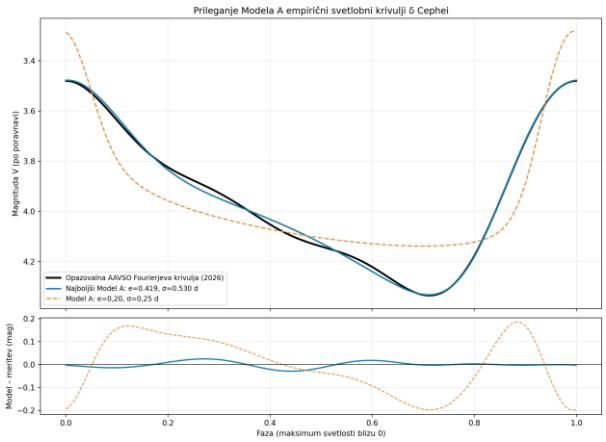


Figure 2. Three-harmonic AAVSO-derived Johnson-V Fourier template for δ Cephei (black), preferred c+u arrival-time model (blue), and an earlier narrower-pulse test (dashed orange). Lower panel: magnitude residuals. The preferred model has RMS ≈ 0.013 mag relative to the empirical template. The Fourier template is observationally derived, whereas the orbital model is hypothetical.

7.4 Sensitivity to pulse width and background flux

The fitted Gaussian width is important because increasing σ widens the observed pulse, reduces its peak concentration and changes the amount of additional light required to keep a specified full amplitude. At an earlier fixed eccentricity e=0.20 and amplitude 0.89 mag, increasing σ from 0.15 to 0.40 d reduced the needed normalized constant contribution from approximately 2.67 to 1.01. The final fit differs because eccentricity was reoptimized against the empirical Fourier profile rather than held at the earlier value.

σ (days)	C/L_A at e=0.20	Pulse FWHM (days)
0.15	2.667	0.435
0.20	2.058	0.580
0.25	1.666	0.722
0.30	1.388	0.863
0.40	1.010	1.136

These sensitivity values describe model dependence and should not be interpreted as a unique estimate of a disk luminosity. They also illustrate why it is essential to fit pulse width and any constant contribution together, rather than determining background light from an unsmoothed caustic alone.

7.5 Sensitivity to a faint luminous B

We also computed the separate arrival-time curve of body B and introduced a small direct flux L_B/L_A. For the fixed best orbital shape, a fraction near 0.7% gave an almost indistinguishable improvement of the RMS (approximately 0.01292 mag compared with 0.01302 mag when B is dark). Larger contributions added unwanted structure and worsened the match. We therefore retain B as optically dark in the representative solution, without claiming that a nearby body would literally reflect no radiation in nature.

8. Physical Interpretation and Independent Observational Checks

8.1 What has been reproduced

For the selected input masses, distance and c+u kinematics, the model provides a quantitatively specified arrival-time curve with the same adopted photometric period as δ Cephei, the same fitted mean V amplitude as the public Fourier reconstruction, and a closely similar asymmetric shape. The comparison demonstrates that kinematic arrival-time concentration can be tuned to imitate an important photometric property of the prototype Cepheid within the assumed propagation framework.

8.2 What remains outside the photometric demonstration

A successful phase-folded brightness fit does not determine whether the actual radiation propagates according to c+u, whether the proposed component masses are realistic, or whether the observed angular-diameter and spectral variations can be reproduced by the same physical system. These are additional constraints rather than minor residuals. In particular, standard Cepheid analyses combine optical light curves with temperature, spectra, radius indicators and radial-velocity measurements [3–6].

8.3 Spectroscopic radial velocity as a quantitative discriminant

The chosen orbit has a small line-of-sight velocity amplitude because it is viewed almost face-on. The model predicts barycentric radial velocities of A ranging approximately from −0.694 to +0.284 km s^{-1}, i.e. a peak-to-peak variation of only 0.978 km s^{-1}. Spectroscopic velocity excursions reported for δ Cephei are of order several tens of km s^{-1}. Thus a direct identification of the observed spectral-line velocity with the orbital radial velocity of A would produce a major discrepancy.

A compound emission environment may, in principle, complicate which component contributes particular spectral lines. Such an explanation requires a line-formation and radiative-transfer model, not an untested assignment of the measured spectrum to the disk. The present paper does not claim to reproduce spectroscopic velocity curves. This issue is an explicit target for future falsification or refinement, and the available velocity discrepancy must remain visible when assessing the overall physical plausibility of the system.

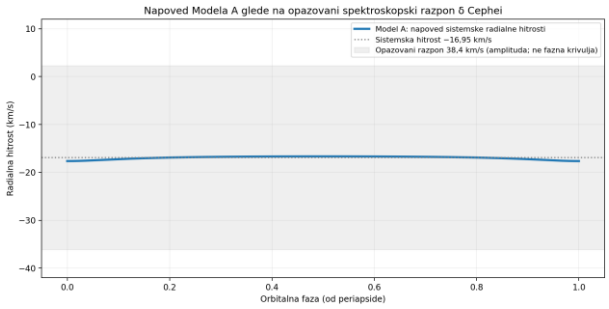


Figure 3. Barycentric line-of-sight velocity predicted for component A by the selected near-face-on Keplerian orbit. The shaded band indicates the scale of the reported spectroscopic velocity variation, not phase-matched measurements. The comparison highlights an unresolved independent constraint.

8.4 Photometric template, raw scatter and prediction

The quoted 0.013-mag RMS compares two smooth phase curves after free alignment and calibration. It is therefore a morphology-matching score and cannot be interpreted as an observational error bar or the probability that the system has the proposed structure. A stronger validation would hold the inferred model parameters fixed and predict independent datasets: additional Johnson-V seasons, a different photometric band, times of individual maxima, radial-velocity line profiles, and wavelength-dependent interferometric visibilities.

8.5 The period–luminosity relation

Any generalization from one prototype star to Cepheids as a population will ultimately need to explain the observed period–luminosity relation. In the present orbital hypothesis, the Keplerian period is linked to total mass and binary semimajor axis, whereas observed luminosity depends on component properties and surrounding emission. Without a derived relation connecting these quantities across a population, the present one-star demonstration does not provide an alternative derivation of the established Cepheid distance scale.

9. Discussion

9.1 Minimality of the illustrative configuration

A central purpose of the study is to avoid making an increasingly elaborate multi-star system solely to improve a photometric curve. A bright Keplerian emitter, a faint gravitating companion and a small unresolved background contribution are sufficient to obtain the fitted morphology. Further dark stabilizers and a detailed distribution of many luminous orbiters are not required for this central calculation. Whether a realistic circumstellar environment could supply the needed flux and observed apparent size is an astrophysical follow-up rather than a premise that must be settled by the photometric fit.

9.2 Gaussian width as an effective observable

The broadening parameter σ≈0.530 d condenses unresolved details of source geometry and motion into a single width. Tests with rigid rotation and linear limb darkening showed how physically motivated velocity kernels change the pulse, but did not replace the Gaussian fit at the same accuracy. The Gaussian choice is therefore operational: it captures the observed smoothness

without selecting among many possible surface distributions. Future physical models should predict the width and its wavelength dependence rather than assuming it.

9.3 Extent and brightness of the hypothetical disk

A disk with a steeply declining radial brightness profile can have a material outer edge substantially beyond the optical region dominating its total flux. This observation is useful when interpreting apparent size, but detailed complex visibility functions and actual flux ratios are needed for a meaningful interferometric comparison. The model's inferred faint constant component is also not automatically passive reflected light: energy conservation bounds the light that can be reprocessed from A. A defensible disk model must satisfy dynamics, radiation balance and observational visibility simultaneously.

9.4 Model limitations and possible decisive tests

The light-curve fit is conditional on ballistic c+u transport. Because conventional vacuum electrodynamics does not predict a source-dependent light speed of this form, direct propagation tests remain decisive. Independently, the spectral-velocity contrast and phase-dependent stellar angular diameter place strong restrictions on the proposed identification of δ Cephei with a near-face-on compact binary. These restrictions do not alter the mathematical result of the conditional fit, but they limit the physical conclusion one may draw from it.

The most informative near-term tests would be: (a) a joint fit of light-curve shape and individual cycle timing using physically fixed orbital parameters; (b) a forward model of spectra from all proposed emitting regions; (c) a synthetic interferometric visibility calculation for a central pair plus radially structured disk; and (d) a prediction of color variation and multi-band light curves from the same physical luminosity and temperature assumptions. These tests could identify which aspects of the photometric degeneracy are genuine and which are excluded by independent data.

9.5 Relation to earlier Part D work

The wider Part D series investigates whether structured electromagnetic propagation and magnetic deflection can affect the apparent behavior of astronomical sources. The present D5 article examines a different, sharply defined arrival-time mechanism: a periodically accelerated source can generate an observer-dependent brightness pattern under the c+u assumption. Connections to the magnetic deflection model of Part D3 and to the sunspot discussions of Part D4 should be treated as part of the broader conceptual motivation. No magnetic focusing coefficient from D3 is needed in the present numerical fit; the result can therefore be evaluated on its own defined assumptions.

10. Conclusions

1. We have constructed a fully specified illustrative eccentric Keplerian binary whose emitting component A produces a strongly asymmetric periodic received-flux profile through a proposed c+u arrival-time map. In this framework the observed periodic brightness does not require an imposed periodic variation of the intrinsic optical power of A.

2. When the model is broadened with a periodic Gaussian response and a faint constant flux, it can be adjusted to the three-harmonic empirical Johnson-V template of δ Cephei. The selected parameters are P=5.366531 d, e≈0.419, inclination≈0.338°, σ≈0.530 d and constant flux C≈0.225 times the mean A contribution. The resulting template-level RMS difference is about 0.013 mag.

3. The Gaussian width is retained as an effective description of unresolved differences in arrival time. Nonuniform surface brightness, rotation, limb darkening and other projected-velocity distributions may contribute, but no unique physical mechanism for σ has been established in the present analysis.

4. A weak circumstellar or unresolved component can reduce the relative photometric amplitude and may influence inferred size, yet its radiation

budget, stability and detailed interferometric appearance have not been established. Matching an optical phase curve does not by itself establish the actual architecture of the star.

Appendix A. Reproduction of the Numerical Light Curve

The following algorithm defines the numerical test sufficiently to be implemented in a conventional programming language. Units should be consistent throughout, with distances in meters and orbital times in seconds except when explicitly converted to days.

1. Select masses M_A , M_B , orbital period P, eccentricity e and adopted distance D. Compute a and a_A from Kepler's law.

2. Sample emission times uniformly over one full period, compute mean anomalies, and solve E−e sin E=M for each sample.

3. Obtain x_A(t), u_A(t) and a_los(t) from Equations (5)–(7). Choose inclination so that max(a_los)=1.05c^2/D.

4. Calculate the stable arrival-time offset δt=−(c x_A + D u_A)/[c(c+u_A)], then fold t+δt into the orbital period.

5. Histogram the transformed times with equal emission weights. Divide by the mean histogram count to normalize the stellar response to unit mean.

6. Convolve the periodic normalized histogram with a Gaussian of trial width σ; add the trial non-negative constant C.

7. Convert fluxes to magnitudes. Determine the optimal circular phase shift and magnitude zero point relative to the observed Fourier template.

8. Search eccentricity and σ; for each trial adjust C to the empirical full amplitude and select the smallest phasewise magnitude RMS.

9. Retain the best-fit curve, all fitted parameters and the model-vs-template residuals. Repeat the comparison with independent observations before interpreting the parameters physically.

A.1 Observational Fourier coefficients

For direct reproducibility, the reference coefficients are c0=3.903085; (c1,s1)=(-0.242286,-0.243384); (c2,s2)=(-0.133974,-0.049481); (c3,s3)=(-0.052745,+0.006366). They refer to the three-harmonic empirical Johnson-V phase curve published in [2].

A.2 Numerical precision and limitations

The global distance term D/c should not be subtracted numerically from a second nearly equal astronomical travel time. Instead Equation (12) must be used directly. The histogram and convolution must be sufficiently fine that changing the bin count and the emission sample count produces negligible change in the fitted RMS. Our comparison is a phase-folded fit to a smooth published template. It does not include full observational covariance, uncertainties in masses or distance, or an independent model for the disk and the line-forming atmosphere.

References

[1] American Association of Variable Star Observers (AAVSO). "Delta Cephei." Variable Star of the Season. https://archive.aavso.org/vsots_delcep/ (accessed November 2026).

[2] Elahi, Z., and Gull, W. (2026). "A Reproducible AAVSO Johnson-V Fourier Template for the Prototype Cepheid Delta Cephei." arXiv:2606.29543. https://arxiv.org/abs/2606.29543.

[3] Mérand, A., et al. (2015). "Cepheid distances from the SpectroPhoto-Interferometry of Pulsating Stars (SPIPS): Application to the prototypes δ Cephei and η Aquilae." Astronomy & Astrophysics 584, A80. https://doi.org/10.1051/0004-6361/201525954.

[4] Armstrong, J. T., et al. (2001). "Diameters of δ Cephei and η Aquilae Measured with the Navy Prototype Optical Interferometer." Astronomical Journal 121, 476–483. (Published mean angular diameter of δ Cephei ≈1.520 mas.)

[5] Nardetto, N., et al. (2016). "VEGA/CHARA interferometric observations of Cepheids. I. A resolved structure around the prototype classical Cepheid δ Cep in the visible spectral range." Astronomy & Astrophysics. https://doi.org/10.1051/0004-6361/201528005.

[6] Gallenne, A., et al. (2016). "Multiplicity of Galactic Cepheids from long-baseline interferometry – III. Sub-percent limits on the relative brightness of a close companion of δ Cephei." Monthly Notices of the Royal Astronomical Society 461, 1451–1462. https://academic.oup.com/mnras/article/461/2/1451/2608480.

[7] Matthews, L. D., et al. (2012). "New Evidence for Mass Loss from δ Cephei from H I 21 cm Line Observations." Astrophysical Journal 744, 53. https://doi.org/10.1088/0004-637X/744/1/53.

[8] Holman, M. J., and Wiegert, P. A. (1999). "Long-Term Stability of Planets in Binary Systems." Astronomical Journal 117, 621–628.

[9] Simon, N. R., and Lee, A. S. (1981). "The Structural Properties of Cepheid Light Curves." Astrophysical Journal 248, 291–297.

[10] Nardetto, N., et al. (2017). "HARPS-N high spectral resolution observations of Cepheids. I. The Baade-Wesselink projection factor of δ Cep revisited." Astronomy & Astrophysics. https://doi.org/10.1051/0004-6361/201629400. (Reported full RV amplitude ≈38.4 km s^{-1}.)